Structural and photochemical properties of Fe-doped ZrO2 and their application as photocatalysts with TiO2 for chromate reduction

N. Doufar, M. Benamira, H. Lahmar, M. Trari, I. Avramova, M.T. Caldes

Structural and photochemical properties of Fe-doped ZrO_2 and their application as photocatalysts with TiO_2 for chromate reduction

N. Doufar [1], M. Benamira [1,4*], H. Lahmar [2], M. Trari [2], I. Avramova [3], M.T. Caldes [4]

[1]*Laboratory of Materials Interaction and Environment-LIME, University of Mohamed Seddik Ben YahiaJijel, Algeria*

[2]*Laboratory ofStorage and Valorization of Renewable Energies, Faculty of Chemistry, USTHB, Algiers, Algeria.*

[3]*Institute of General and Inorganic Chemistry, Bulgarian Academy of Sciences, Block 11, Acad. G. Bonchev Str., 1113 Sofia, Bulgaria*

[4]*Institut des Matériaux Jean Rouxel (IMN), Université de Nantes, CNRS, 2, Rue de la Houssinière, BP 32229, 44322 Nantes cedex 3, France*

** Corresponding author: m_benamira@univ-jijel.dz; benamira18@yahoo.fr*

Abstract

In this work, we are interested by the photocatalytic activity under sunlight irradiation of Fe-doped ZrO_2 prepared by co-precipitation. The structural and photophysical properties of the catalysts have been characterized by X-ray diffraction (XRD), scanning electron microscopy (SEM), X-ray photoelectron spectroscopy (XPS), BET method and UV–Vis diffuse reflectance. The results show that Fe-doped ZrO_2 exhibits higher photocatalytic activity than that of both ZrO_2 and commercial TiO_2 P25. The best photocatalytic activity is obtained with the 50 mol% Fe-content calcined at 600 °C/ 3 h. A total photoreduction of Cr(VI) is achieved within 90 min under solar light with the new hetero-junction Fe-ZrO_2/TiO_2. The kinetic of Cr(VI) photoreduction is well described by the Langmuir-Hinshelwood (L-H) model which obeys to pseudo-first-order kinetics with a rate constant of 0.031 min^{-1}. On the basis of the energy band positions of the hetero-junction Fe-ZrO_2/TiO_2, the detailed reaction mechanism of reduction of inorganic pollutant has been discussed.

Keywords: Photoactivity; co-precipitation ZrO_2; Cr(VI) reduction; XRD; Solar irradiation.

1. Introduction

In the last two decades, the protection of the environment has become a major economic issue for all countries. This is due to population growth where our planet has more than 7.5 billion people and an annual growth rate of 1.2%. This increase in the world population requires an intensification of agro-industrial activities in order to meet the growing needs. Therefore, natural resource management has become nowadays a priority, especially, the water which affects our survival and preservation of the planet. Indeed, the water has become a precious resource, rare and even subject to tension and conflicts [1-2]. The reuse of wastewater in the agriculture industry is an encouraging alternative but requires strict specifications for the composition of the polluting water. The removal of pollutants (heavy metals, nitrates, oils, pesticides and dyes) from wastewaters has become an important process of first priority [3-5].

The conventional water treatment processes are not able to be efficient and cost-effective. In this respect, the photocatalysis is an alternative and inexpensive technique, which does not need any special set up and activities under soft conditions, close to natural medium [6-8]. In this regard, many semiconductor oxides (SC) were used to eliminate a variety of inorganic and organic pollutants [9-10]. Nevertheless, the electronic bands of many oxides are misplaced and cannot cover the redox levels in solution. To overcome these disadvantages, the search of active photocatalysts in the visible region is necessary.

In this work, we are interested by the photocatalytic reduction of the toxic chromate, widely used in many industries like electroplating, leather tanning, batteries and the manufacture of steel. Most of the chrome eventually settles and ends up in water or soil. Man is exposed to chromium by breathing, eating, drinking or skin contact and the hexavalent state is dangerous for the human health. The photocatalyts used in this study are composed of Fe-doped ZrO_2. Zirconia (ZrO_2) is a material whose use is growing as thermal barrier coatings (TBCs) [11-13], electrolyte for solid oxide fuel cells [14-16], medical field [17-19] and heterogeneous catalysis [20-22]. Kaliaraj et al. studied the corrosion behavior of monoclinic and tetragonal ZrO_2 coating for biomedical applications [17]. Because of its nature as *n*-type

semiconductor, it is used as a photocatalyst for the degradation of both organic and inorganic pollutants in water [23-27]. The band gap energy (E_g) of ZrO_2 reported in the literature lies between 3.3 and 5.2 eV, largely depending on the synthesis method [25, 28-30]. In the light of this, ZrO_2 is doped by different Fe-content in order to improve the photocatalytic properties by decreasing the band gap and shifting the absorption toward the visible light region. To our knowledge, Fe-ZrO_2 has the subject of several studies but its photoelectrochemical properties (PEC) has not been exploited yet.

The main objective is to use sunlight for the total degradation of inorganic pollutant (Cr(VI)). To achieve this goal, the solution is to use hetero-junction by introducing other materials such as TiO_2. The p-n hetero-junction Fe-ZrO_2/TiO_2 is built in order to reduce the recombination of electron/hole (e^-/h^+) pairs and to improve the photocatalytic performance. By properly positioning the conduction bands of both Fe-ZrO_2 and TiO_2 semiconductors, the energy band diagram of the injection process can be obtained. Indeed, The photoelectrons of Fe-ZrO_2 -CB (-2.19 V_{SCE}) is negative enough to be injected to $HCrO_4^-$. The Fe-ZrO_2 photocatalysts have been prepared by the co-precipitation and characterized by different techniques for a better knowledge about the photocatalytic properties. Finally, the energy band diagram at the hetero-junction of Fe-ZrO_2/TiO_2 was determined to support the proposed mechanism of reduction of inorganic pollutant.

2. Experimental

Fe-doped ZrO_2 (3 g) was synthesized byco-precipitation using $ZrOCl_2{\cdot}8H_2O$ (99.5%; Sigma–Aldrich), $FeCl_3{\cdot}6H_2O$ (97%; Sigma–Aldrich) and NH_4OH as starting materials. All the starting reagents were of analytical grade and mixed in amounts according to following stoichiometric equation:

$$(1\text{-}x)\ ZrOCl_2.8H_2O + x\ FeCl_3.6H_2O + (2+x)\ NH_4OH \rightarrow Zr_{(1-x)}Fe_xO_{(2-x/2)} + (2+x)\ NH_4Cl + 18\ H_2O \quad (x = 0.0, 0.05, 0.1 \text{ and } 0.5)$$

An appropriate amount of $ZrOCl_2{\cdot}8H_2O$ was dissolved in distilled water (100 mL) and stirred vigorously for 30 min. After that, three amounts of $FeCl_3{\cdot}6H_2O$ were added to the first

solution. The calculated amount of the corresponding $ZrOCl_2 \cdot 8H_2O$ and $FeCl_3 \cdot 6H_2O$ are listed in Table 1. The aqueous suspensions were mixed and stirred slowly for 45 min at 65 °C. NH_4OH (2.5 M) was added drop wise under continuous stirring for 60 min to adjust the pH solution at 10, and to form a solid precipitate with a brown color. The resulting mixture was centrifuged for 20 min to collect the precipitate which was filtered and washed several times with deionized water. The resulting precipitate was then dried in an oven at 100 °C for 24 h and calcined at 600 °C for 3 h. Undopoed ZrO_2 (3 g) was also prepared by co-precipitation as reported in the literature [28, 30]. The white powder obtained after drying in air oven at 100°C (12 h) was calcined under air at 600 °C (3 h). TiO_2 powder used in the hetero-junction was synthesized as reported by Bessekhouad et al. [31]. The method consists of dissolving $Ti(OC_3H_7)_4$ in methanol/ethanol solution in a molar ratio (1/1/10) and stirring for 3 h at 75 °C. The gel was dried overnight and heated at 450 °C for 2 h. The hetero-junction Fe-ZrO_2/TiO_2 was obtained by mixing both catalysts in the mass ratio (1/1). Commercial TiO_2 P25 powder (75 wt% anatase and 25 wt% rutile) with a specific surface area of 50 m^2 g^{-1} and an average particle sizes of 20 nm was purchased from Degussa (Germany) and used for a comparison purpose.

X-ray diffraction (XRD) was used to characterize the structure of the as prepared powders. The patterns were obtained using a Brüker"D8 Advance" powder diffractometer with a Cu Kα radiation (λ = 1.54056 Å) and 2θ varying from 20 to 90° by steps increments of 0.0146° and 0.2 s counting time per step. The Scanning Electron Microscopy (SEM) was performed on a FEG-SEM JEOL 7600 in order to evaluate the size distribution as well as the morphology of the nanoparticles. We sprinkle a little of the powder evenly but lightly on a SEM sample stub with the double-sided sticky carbon tape. The hand blower was used to blow away the loose particles. The X-ray photoelectron spectrometry (XPS) was performed on a Kratos AXIS Supra spectrometer with a non-monochromatic Al X-ray source under vacuum (< 10^{-8} Pa) at 90° take-off angle. Each analysis started with a survey scan from 0 to 1200 eV, pass energy of 160 eV at steps of 0.5 eV with 1 sweep. For the high resolution analysis, the number of sweeps was increased while the pass energy was lowered down to 20 eV (steps: 100 meV). The XPS spectra were calibrated in binding energy with C 1s (285 eV). The C1s, O1s, Zr3d and Fe*2p* lines were recorded for each specimen and further on, the O1s and Fe2p lines were subjected to additional fitting procedure with XPSPEK4.1 software. The

FT-IR spectra were recorded on a VERTEX 70/70v spectrophotometer (BRUKER) in transmission mode between 400 and 4000 cm^{-1}.

The UV–vis diffuse reflectance spectrawereobtainedwith a UV-visible spectrophotometer (Specord 200 Plus).The BET surface areas of the powderswere carried out on a Micromeritics 3Flex analyzer determined by N_2adsorption–desorption isotherm measurement at -196 °C.The electrochemical characterization was performed in 0.1 M Na_2SO_4 electrolyte using a standard three-electrode cell usingSolartron 1287 potentiostat and frequency response analyzer Solartron 1260; the sweep rate was set at 5 mVs^{-1}. The interfacial capacitance of the photocatalyst was studied at a fixed frequency of 10 kHz. The working electrode is prepared as 11 mm diameter pellet using uniaxial pressure of 4 MPa and sintered at 600°C for 2 h. It was introduced into resin epoxy, polished with SIC paper (1200) and washed with water, only one side (1 cm^2) is in contact with the electrolyte. The electrical contact was achieved by the painted silver lacquer. The electrical conductivity (σ) measurements were performed by the two-probe technique over the temperature range (300 - 500 K).

The photocatalytic tests were conducted in June between 10 am and 3 pm outside our laboratory (LIME). The sunlight irradiation was evaluated as 700 W/m^2, while the temperature averaged 27 °C. The photocatalytic tests were carried out in an open Pyrex glass reactor with a double wall. Before irradiation, the suspensions composed of 50 mL of Cr(VI), 50 mg of catalyst and oxalic acid (10^{-5} M) were kept in the dark for 60 min under magnetic stirring to ensure good adsorption equilibrium on the catalyst surface. Then, the reactor was exposed to solar irradiation. The absorbance was measured with a UV-visible spectrophotometer (Shimadzu UV-2400). After irradiation, the Cr(VI) solutions were centrifuged and filtered through a membrane filter in order to measure the decomposition rate.

3. Results and discussion

3.1 Characterization of material

Fig. 1 shows the XRD patterns of Fe-doped ZrO_2 synthesized by co-precipitation. ZrO_2 calcined at 600°C shows that all peaks belong to the monoclinic phase (m-ZrO_2) with space group P21/c (JCPDS Card N° 07-0343). The substitution of Zr by Fe (5 and 10 mol%) confirms the formation of the tetragonal solid solution $Zr_{1-x}Fe_xO_{2-x/2}$ in agreement with JCPDS

Card N° 17-0923. The incorporation of higher Fe content (50 mol%) reveals the presence of new peaks of the hematite (α-Fe_2O_3, JCPDS N° 01-1053) and confirms the results obtained by Davison et al. [32], Abraham et al. [33] and Botta et al. [34]. The substitution of Zr^{4+} by Fe^{3+} ions in the ZrO_2 lattice was reported using different preparation methods. The authors investigate the stabilization of the ZrO_2 cubic structure by 2.5-40 at% of Fe^{3+} at the same calcination temperature than this work [32]. The study confirms the formation of tetragonal phase at low Fe^{3+} concentrations (<10 at%) with the absence of XRD peaks of α-Fe_2O_3. However, for high Fe^{3+} content (> 20 at%), the XRD patterns indicate the presence of α-Fe_2O_3 phase, which is in total agreement with our results.

Fig. 2 shows the FEG-SEM images of the synthesized powder. Uniform spherical shape and size of nanoparticles of ZrO_2 are obtained with an average nanoparticle sizes less than 50 nm. The powders with Fe content present large agglomerate grains whose is less uniform with the presence of large and small compact grains. Furthermore, a very fine agglomerated powder is observed and is difficult to be distinguished among the different particles constituted the grains. For powder with high content of iron (Fig. 2d), we can observe round the surface of large grains, attributed to α-Fe_2O_3. This observation confirms the XRD analysis and is reported also in the study of De Resende et al. [35].

The specific surface areas of the as-prepared TiO_2 and $Zr_{1-x}Fe_xO_{2-x/2}$ powders (x = 0.05, 0.10 and 0.5) were determined using the N_2 adsorption–desorption isotherm as a function of relative pressure (P/P_o) between 0.05 and 0.32; the BET surface areas are listed in Table 2. We can observe that the substitution of Zr by Fe increases the surface area; nevertheless, this increase is not too high. The addition of 5 mol% Fe to ZrO_2 increases the surface area from 25.25 to 29.02 $m^2\ g^{-1}$. After that, the increase of the surface area is too small with values lying between 30.02 and 31.88 $m^2\ g^{-1}$ for 10 and 50 mol% of Fe, respectively and this should improves slightly the photocatalytic activity. The co-precipitation method allowed us to have a high specific surface area between 25.25 $m^2\ g^{-1}$ for ZrO_2 and 31.88 $m^2\ g^{-1}$ for $Zr_{1-x}Fe_xO_{2-x/2}$ (x= 0.5). The specific surface area of the TiO_2 powder used in the hetero-junction was 30.21 $m^2\ g^{-}1$.

The Fourier transform IR spectra of $Zr_{1-x}Fe_xO_{2-x/2}$ recorded between 500 and 4000 cm^{-1} are shown in Fig. 3. The peaks observed below 750 cm^{-1} are attributed to the M–O bonds, Zr–O

and Fe-O stretching vibrations [36]. A stronger band in the region (3250-3600 cm^{-1}) corresponds to the O–H stretching vibration while the peaks at 1470 and 1560 cm^{-1} are assigned to adsorbed water molecules (Fig. 3b) [37]. A weak peak at 2320 cm^{-1} is assigned to adsorbed carbon dioxide when the sample was handled in air.

The surface compositions of $Zr_{1-x}Fe_xO_{2-x/2}$ (x= 0.0 and 0.5) and the chemical states of constituent elements have been studied by XPS. The O1s photoelectron lines of oxides are showninFig.4. The O1s for ZrO_2 (Fig. 4b) was fitted with two components. The first one at 530.17 eV belongs to oxygen from the lattice while the second one (531.71 eV) is due to defects or OH^- groups on the oxide surface [38-39]. The O1s photoelectron peaks for $Zr_{1-x}Fe_xO_{2-x/2}$ (x= 0.5) are slightly shifted to lower binding energies (Fig. 4c), confirming the substitution of Zr^{4+} ions by Fe^{3+}. The first peak is shifted to 529.70 eV i.e. a displacement is 0.47 eV. The second peak is shifted to 531.31 eV (0.40 eV). The same trend was observed for the Zr3d photoelectron line (Fig. 4e), where the binding energy values (182.33 and 184.73 eV) and separation (2.4 eV) determined in the Zr3d spectrum of ZrO_2 are due to $Zr3d_{5/2}$ and $Zr3d_{3/2}$ emissions of Zr^{4+} sites [38]. The Zr3d photoelectron peaks for $Zr_{1-x}Fe_xO_{2-x/2}$ (x= 0.5) are slightly shifted to lower binding energies. The first and second peaks are shifted to 181.96 and 184.36 eV, respectively. The value of this displacement is 0.4eV, which is more less the same to that obtained in the case of O1s. It was also noticed that the intensities of $Zr3d_{5/2}$ and $Zr3d_{3/2}$ decrease with Fe doping. The Fe2p photoelectron line is complex and was also deconvoluted; the three peaks of Fe2p observed at 711.1, 719.3 and 724.3 are characteristic of Fe^{3+} obtained from Fe_2O_3 [40] and confirms the XRD analysis about the presence of α-Fe_2O_3 for the high Fe content (50 mol%). The insertion of Fe^{3+} cation in the ZrO_2 lattice favors the formation of oxygen vacancies, as reported by the density functional theory (DFT) of Y^{3+} doped ZrO_2 [41].

The diffuse reflectance spectra of $Zr_{1-x}Fe_xO_{2-x/2}$, ZrO_2 and TiO_2 are shown in Figs 5a and 5b. The converted UV-visible absorption data are used to evaluate the optical band gap (E_g) of $Zr_{1-x}Fe_xO_{2-x/2}$ by extrapolating the linear portion of the plots $(\alpha h\nu)^2$ versus $h\nu$to $(\alpha h\nu)^2 = 0$. It can be observed that the optical band gap decreases from 2.15 eV (x=0.05, $Zr_{0.95}Fe_{0.05}O_{1.975}$) to 1.77 (x=0.5) (Table 1). The same behavior was obtained by Kambur et al. [42] in the photoactivity of binary system ZrO_2-TiO_2 in which E_g increases from 3.10 to 3.25 eV with

decreasing the amount of TiO_2. The insertion of Fe^{3+} in the ZrO_2 lattice decreases the gap and allows the new compounds to absorb the sunlight more than ZrO_2, TiO_2 and α-Fe_2O_3, making them more attractive for photocatalytic applications.

3.2. Photocatalytic activity and kinetic study

The photocatalytic activities of $Zr_{1-x}Fe_xO_{2-x/2}$ catalysts are compared with TiO_2 P25, presented as the one of the efficient (photocatalyst/photocatalysts). The chromate reduction of the working solution ($HCrO_4^-$, 30 mg/L) on different photocatalysts (dose = 1 mg/mL, pH ~ 4, T = 25 °C) is illustrated in Fig. 6a in the presence of oxalic acid as hole scavenger. One can see that pure m-ZrO_2 and TiO_2 P25 present a low photocatalytic activity under solar light irradiation. These results can be explained by their large band gap, 4.01 and 3.21 eV respectively, which limits the photoactivity to the UV light. Fig. 6a shows also the effect of Fe-doping, the photocatalytic reduction of Cr(VI) is still higher than that of m-ZrO_2 and TiO_2 P25 and increases with increasing the Fe-content in the sample, 50 % of Cr(VI) was reduced after 90 min. The introduction of Fe^{3+} in the zirconia structure increases the concentration of oxygen vacancies and consequently enhances the photocatalytic efficiency.

The use of the hetero-junction system is one of the effective ways to improve the photocatalytic activity under visible light irradiation. Fig. 6b shows the UV–visible spectra of Cr(VI) solutions in the presence of 50 mol%Fe-ZrO_2/TiO_2 hetero-junctionwith a mass ratio (1/1) under solar light irradiation. A rapid decrease of Cr(VI) absorption intensity peak over irradiation time at 350 nm is observed, indicating a better photodegradation on the hetero-junction. Furthermore, 100% of Cr(VI) is reduced in less than 90 min (Fig. 6a), attesting the high photocatalytic activity of the new hetero-junction.

The Cr(VI) concentration in wastewater often exceeds 30 mg/L. At this stage, it is important to study the effect of the initial concentration of Cr(VI) solutions on the photo-reduction using the hetero-system 50 mol%Fe-ZrO_2/TiO_2 (Fig.7a). The amount of Cr(VI) reduction increases with augmenting $C_o$with a maximum of 50 % of Cr(VI) reduced after 90 min in the case of 75 mg/L. In contrast, the reduction rate decreases with increasing C_o. At low concentrations, the number of the surface active sites is higher than that of Cr(VI) ions and can explain the complete reduction. On the contrary, the number of Cr(VI) ions becomes

higher than that of photocatalytic sites at high concentration and the photoactivity decreases again; an optimal concentration of 30 mg/L with a total reduction of Cr(VI) was obtained within 90 min. The Cr(VI)reduction rate obeys to a pseudo-first order kinetic:

$$\mathrm{Ln}\left(\frac{C_0}{C}\right) = k_{app}\, t \qquad (1)$$

k_{app} (min^{-1}) is the apparent rate constant, C_o and C are respectively the initial concentration and the concentration at time (t).

Fig. 7b shows the plot of Ln (C_o/C) vs.timefor different Cr(VI)concentrations. The line fits well the experimental data and theapparent rate constants k_{app}decreases with the increase of C_o (Table 3). The kinetic of the Cr(VI) reduction on the new hetero-junction follows the L-H model [43].

$$\frac{1}{k_{app}} = \frac{1}{k_r k_s} + \frac{C_o}{k_r} \qquad (2)$$

k_r and k_s are respectively the reaction rate and adsorption constant.

The linear plot $1/k_{app}$vs. C_o (Fig. 7b Insert) allows us to calculate the constants k_r (3.2375 mg L^{-1} min^{-1}) and k_s (0.3637 L mg^{-1}). It can be seen that the photoactivity decreases with time and can be attributed to the blocking of the photo-electrochemical sites by $Cr(OH)_3$ owing to its low solubility (5.4×10^{-31}) and can be precipitate for pH> 5. Another explanation is that the Cr(VI) reduction may in competition by the water reduction reaction [44].

The position of the conduction and valence bands of each catalyst on the energy band diagram is the best way to predict and explain the reaction mechanism of the photoreduction of Cr(VI) over the new hetero-system Fe-ZrO_2/TiO_2. The valence band position of 50 mol%Fe-ZrO_2 is calculated as reported in our previous studies [44-46].

$$E_{VB} = 4.75 + E_{fb} + 0.059(pH - pH_{pzc}) + E_a \qquad (3)$$

Where E_a(= 0.15 eV) is the activation energy obtained from the plot log (electrical conductivity) vs. temperature (Fig. 8b), confirming a semiconductor behavior of the sample. The point of zero charge pH_{pzc} (pH_{pzc}= 6.3) is the pH for which 50 mol% Fe-ZrO_2 exhibits

zero charge on the surface; it was determined at the equilibrium of a solution with an excess of 50 mol%Fe-ZrO_2 powder. The flat band potential E_{fb} (-0.44 V_{SCE}) is obtained from the intercept of the linear part of the plot of the reverse of the capacitance (C^{-2}) vs. the potential (Fig. 8a). The negative slope confirms the *p* type behaviour of 50 mol%Fe-ZrO_2 material.

Fig. 9 shows the energy band diagram of the novel II-type hetero-junction 50 mol% Fe-ZrO_2/TiO_2. The Cr(VI) removal under sunlight irradiation is enhanced by the photocatalytic activity of the hetero-junction and synergistic effects between Fe-ZrO_2 and TiO_2. The band positions of the two photocatalysts match well, and provid the force needed to the transfer of photo-generated carriers, thus facilitating the Cr (VI) reduction.

When the photocatalyst absorbs an energy higher than the gap ($h\nu > E_g$), the CB electrons (e^-_{CB}) and VB holes (h^+_{VB}) are generated. CB of 50 mol% Fe-ZrO_2-CB is positioned below TiO_2-CB (Fig. 9). In such a case, the thermodynamic conditions for a charge transfer between 50 mol% Fe-ZrO_2 and TiO_2 are respected and the improved photoactivity is due to the facility of electrons transfer due to a band bending close to the ideal value of ~ 0.5 V. The photo-induced electrons (e^-_{CB}) on CB of 50 mol% Fe-ZrO_2 (-2.19 V) are injected to that of TiO_2 (TiO_2-CB, -0.98 V) and subsequently transferred to adsorbed Cr(VI) ions inducing the reduction process. As a result, the holes and electrons were separated and accumulated on different photocatalysts. The position of CB and VB of 50 mol% Fe-ZrO_2 and TiO_2 which formed the p-n hetero-junction is favorable for the separation of (e^-/h^+) pairs and reduces the recombination process. This is attributed to the more negative potentials of CB (-2.19 V) and VB (-0.42 V) for 50 mol% Fe-ZrO_2 compared to those of CB (-0.98 V) and VB (2.23 V), for TiO_2. Additionally, the presence of oxalic acid as hole scavenger prevents the charge recombination. The electrons collected on TiO_2-CB layer can reduce Cr (VI) into Cr (III) while the holes collected on 50 mol% Fe-ZrO_2-VB can oxidize H_2O. The detailed reactionsoccurring on the new hetero-junction are the following:

$$\text{Fe-}ZrO_2 + h\nu \rightarrow \text{Fe-}ZrO_2\ (e^-_{CB}, h^+_{VB}) \quad (4)$$

$$\text{Fe-}ZrO_2 + h\nu \rightarrow \text{CB- Fe-}ZrO_2\ (e^-) + \text{VB- Fe-}ZrO_2\ (h^+) \quad (5)$$

$$\text{CB- Fe-}ZrO_2\ (e^-) + n\text{-}TiO_2 \rightarrow \text{Fe-}ZrO_2 + TiO_2\ (e^-) \quad (6)$$

$$TiO_2\ (3\ e^-) + HCrO_4^- + 7H^+ \rightarrow Cr^{3+} + 4\ H_2O + TiO_2 \quad (7)$$

TiO_2 (2 e^-) + 2 H_2O → TiO_2 + H_2 + 2 OH^- (8)

$HCrO_4^-$ + 7 H^+ + 3 e^- → Cr^{3+} + 4 H_2O (9)

2H_2O+ 2 e^- → H_2 + 2 OH^- (10)

$C_2H_2O_4$ + 0.5 O_2 + 4 h^+→ 2 CO_2 + H_2O + 4 H^+ (11)

4. Conclusion

The physicochemical properties of the as-prepared nanoparticles by co-precipitation of $Zr_{1-x}Fe_xO_{2-x/2}$ were studied by physical techniques. The XRD analysis confirmed the formation of the tetragonal $Zr_{(1-x)}Fe_xO_{(2-x/2)}$ solid solution for low Fe-content while the presence of hematite α-Fe_2O_3 was detected for higher Fe-content. The specific surface areas of the prepared powders were between 25.25 and 31.88 m^2 g^{-1}. The optical band gap increased with decreasing the Fe content from 1.77 to 2.15 eV. The photoreduction of Cr(VI) by the system $Zr_{1-x}Fe_xO_{2-x/2}$ under solar light confirmed the high photocatalytic efficiency compared to TiO_2 P25 and undoped ZrO_2. The use of *p-n* hetero-junction improves the photoactivity by enhancing the separation of (electron/hole) pairs and reducing the recombination process. The photocatalytic mechanism of the degradation of hexavaent chromium was proposed. A total photodegradation of Cr(VI) was obtained in less than 90 min.

Acknowledgments

The authors are grateful to the Agence Thématique de Recherche en Sciences et Technologie (ATRST) for Financial support (Projet de mobilité, PM 04/2018 et projet à impact socio-économique).

References

[1]. D.P. Loucks, E. Van Beek, Water resource systems planning and management: An introduction to methods, models, and applications, Springer, 2017.

[2]. P.M. Link, J. Scheffran, T. Ide, Conflict and cooperation in the water-security nexus: a global comparative analysis of river basins under climate change, Wiley Interdiscip. Rev. Water. 3 (2016) 495–515

[3]. G. Crini, E. Lichtfouse, Advantages and disadvantages of techniques used for wastewater treatment, Environ. Chem. Lett. 17 (2019) 145–155.

[4]. A.R. Ribeiro, O.C. Nunes, M.F.R. Pereira, A.M.T. Silva, An overview on the advanced oxidation processes applied for the treatment of water pollutants defined in the recently launched Directive 2013/39/EU, Environ. Int. 75 (2015) 33–51.

[5]. T. Van Son, N. HuuHao, G. Wenshan, Z. Jian, L. Shuang, T. Cuong Ton, Z. Xinbo, Typical low cost biosorbents for adsorptive removal of specific organic pollutants from water, Bioresour. Technol. 182 (2015) 353–363

[6]. P.K.J. Robertson, Semiconductor photocatalysis: an environmentally acceptable alternative production technique and effluent treatment process, J. Clean. Prod. 4 (1996) 203–212.

[7]. M. Mahalakshmi, B. Arabindoo, M. Palanichamy, V. Murugesan, Photocatalytic degradation of carbofuran using semiconductor oxides, J. Hazard. Mater. 143 (2007) 240–245.

[8]. S. Das, V.C. Srivastava, Microfluidic-based photocatalytic microreactor for environmental application: A review of fabrication substrates and techniques, and operating parameters, Photochem. Photobiol. Sci. 15 (2016) 714–730.

[9]. A. Mills, S. Le Hunte, An Overview of Semiconductor Technology, J. Photochem. Photobiol. A Chem. 108 (1997) 1–35.

[10]. K. Nakata, A. Fujishima, TiO2 photocatalysis: Design and applications, J. Photochem. Photobiol. C Photochem. Rev. 13 (2012) 169–189

[11]. M.H. Khajezadeh, M. Mohammadi, M. Ghatee, Hot corrosion performance and electrochemical study of CoNiCrAlY/YSZ/YSZ-La2O3 multilayer thermal barrier coatings in the presence of molten salt, Mater. Chem. Phys. 220 (2018) 23–34.

[12]. F. Saberi, B.S. Boroujeny, A. Doostmohamdi, A.R. Baboukani, M. Asadikiya, Electrophoretic deposition kinetics and properties of ZrO2 nano coatings, Mater. Chem. Phys. 213 (2018) 444–454.

[13]. C. Amaya, J.C. Caicedo, J.M. Yáñez-Limón, R.A. Vargas, G. Zambrano, M.E. Gómez, P. Prieto, A non-destructive method for determination of thermal conductivity of YSZ coatings deposited on Si substrates, Mater. Chem. Phys. 136 (2012) 917–924.

[14]. M. Pastor, S. Maiti, A. Pandey, K. Biswas, I. Manna, Effect of dysprosia doping on structural and electrical property of stabilized zirconia for intermediate- temperature SOFCs, Mater. Chem. Phys. 125 (2011) 202–209.

[15]. M. Benamira, A. Ringuedé, M. Cassir, D. Horwat, P. Lenormand, F. Ansart, J.-M. Bassat, J.-P. Viricelle, Enhancing oxygen reduction reaction of YSZ/La2NiO4+ δ using an ultrathin La2NiO4+ δ interfacial layer, J. Alloys Compd. 746 (2018) 413–420.

[16]. T. Selvaraj, B. Johar, S.F. Khor, Iron/zinc doped 8mol% yttria stabilized zirconia electrolytes for the green fuel cell technology: A comparative study of thermal analysis, crystalline structure, microstructure, mechanical and electrochemical properties, Mater. Chem. Phys. 222 (2019) 309–320.

[17]. G.S. Kaliaraj, V. Vishwakarma, K. Alagarsamy, A.M.K. Kirubaharan, Biological and corrosion behavior of m-ZrO2 and t-ZrO2 coated 316L SS for potential biomedical applications, Ceram. Int. 44 (2018) 14940–14946.

[18]. E. Długoń, K. Pach, M. Gawęda, R. Jadach, A. Wajda, M. Leśniak, A. Benko, M. Dziadek, M. Sowa, W. Simka, Anticorrosive ZrO2 and ZrO2-SiO2 layers on titanium substrates for biomedical applications, Surf. CoatingsTechnol. 331 (2017) 221–229.

[19]. S. Devgan, S.S. Sidhu, Evolution of surface modification trends in bone related biomaterials: A review, Mater. Chem. Phys. 233 (2019) 68–78.

[20]. D. Pietrogiacomi, M.C. Campa, L.R. Carbone, S. Tuti, M. Occhiuzzi, N2O decomposition on CoOx, CuOx, FeOxorMnOxsupported on ZrO2: The effect of zirconia doping with sulfates or K+on catalytic activity, Appl. Catal. B Environ. 187 (2016) 218–227.

[21]. P.M. De Souza, R.C. Rabelo-Neto, L.E.P. Borges, G. Jacobs, B.H. Davis, U.M. Graham, D.E. Resasco, F.B. Noronha, Effect of Zirconia Morphology on Hydrodeoxygenation of Phenol over Pd/ZrO2, ACS Catal. 5 (2015) 7385–7398.

[22]. H.J. Eom, M.S. Kim, D.W. Lee, Y.K. Hong, G. Jeong, K.Y. Lee, Zirconia catalysts (ZrO2 and Na-ZrO2) for the conversion of phenethyl phenyl ether (PPE) in supercritical water, Appl. Catal. A Gen. 493 (2015) 149–157.

[23]. M. Gohin, E. Allain, N. Chemin, I. Maurin, T. Gacoin, J.-P. Boilot, Sol–gel nanoparticulate mesoporous films with enhanced self-cleaning properties, J. Photochem. Photobiol. A Chem. 216 (2010) 142–148.

[24]. S. Sampurnam, S. Muthamizh, T. Dhanasekaran, D. Latha, A. Padmanaban, P. Selvam, A. Stephen, V. Narayanan, Synthesis and characterization of Keggin-type polyoxometalate/zirconia nanocomposites—Comparison of its photocatalytic activity towards various organic pollutants, J. Photochem. Photobiol. A Chem. 370 (2019) 26–40.

[25]. T.V.L. Thejaswini, D. Prabhakaran, M.A. Maheswari, Synthesis of mesoporous worm-like ZrO2–TiO2 monoliths and their photocatalytic applications towards organic dye degradation, J. Photochem. Photobiol. A Chem. 344 (2017) 212–222.

[26]. J.A. Navio, G. Colón, J.M. Herrmann, Photoconductive and photocatalytic properties of ZrTiO4. Comparison with the parent oxides TiO2 and ZrO2, J. Photochem. Photobiol. A Chem. 108 (1997) 179–185.

[27]. A. V. Emeline, G.N. Kuzmin, L.L. Basov, N. Serpone, Photoactivity and photoselectivity of a dielectric metal-oxide photocatalyst (ZrO2) probed by the photoinduced reduction of oxygen and oxidation of hydrogen, J. Photochem. Photobiol. A Chem. 174 (2005) 214–221.

[28]. S. Kumar, S. Bhunia, A.K. Ojha, Effect of calcination temperature on phase transformation, structural and optical properties of sol–gel derived ZrO2 nanostructures, Phys. E Low-Dimensional Syst. Nanostructures. 66 (2015) 74–80.

[29]. J. Zhang, L. Li, S. Wang, T. Huang, Y. Hao, Y. Qi, Multi-mode photocatalytic degradation and photocatalytic hydrogen evolution of honeycomb-like three-dimensionally ordered macroporous composite Ag/ZrO2, RSC Adv. 6 (2016) 13991–14001.

[30]. J.A. Navio, M.C. Hidalgo, G. Colon, S.G. Botta, M.I. Litter, Preparation and Physicochemical Properties of ZrO2 and Fe/ZrO2 Prepared by a Sol− Gel Technique, Langmuir. 17 (2001) 202–210.

[31]. Y. Bessekhouad, D. Robert, J. V. Weber, Preparation of TiO_2 nanoparticles by sol-gelroute, International Journal of Photoenergy 5 (2003) 153-158.

[32]. S. Davison, R. Kershaw, K. Dwight, A. Wold, Preparation and characterization of cubic ZrO2 stabilized by Fe (III) and Fe (II), J. Solid State Chem. 73 (1988) 47–51.

[33]. A.G. Abraham, A. Manikandan, E. Manikandan, S.K. Jaganathan, A. Baykal, P. Renganathan, Enhanced Opto-Magneto Properties of Ni x Mg1–x Fe2O4 (0.0≤ x≤ 1.0) Ferrites Nano-Catalysts, J. Nanoelectron. Optoelectron. 12 (2017) 1326–1333.

[34]. S. Botta, J. Navío, M. Hidalgo, 34. Photocatalytic properties of ZrO 2 and Fe/ZrO 2 semiconductors prepared by a sol–gel technique, J. Photochem. Photobiol. A Chem. 129 (1999) 89–99

[35]. V.G. De Resende, F.L. Garcia, A. Peigney, E. De Grave, C. Laurent, Synthesis of Fe-ZrO2 nanocomposite powders by reduction in H2 of a nanocrystalline (Zr, Fe) O2 solid solution, J. Alloys Compd. 471 (2009) 204–210.

[36]. F. Gözüak, Y. Köseoğlu, A. Baykal, H. Kavas, Synthesis and characterization of CoxZn1−xFe2O4 magnetic nanoparticles via a PEG-assisted route, J. Magn. Magn. Mater., 321 (2009) 2170-2177.

[37]. R. Frost, H.Y. Zhu, P. Wu, T. Bostrom, Synthesis of acicular goethite with surfactants, Mater. Lett., 59 (2005) 2238-2241.

[38]. A. Salaün, M. Veillerot, F. Pierre, E. Souchier, V. Jousseaume, ZrO2 thin film deposition on TiN by plasma enhanced atomic layer deposition Using cyclopentadienyltris (dimetylamino) zirconium, ECS J. Solid State Sci. Technol. 3 (2014) N39–N45.

[39]. J. Luo, X. Luo, C. Hu, J.C. Crittenden, J. Qu, Zirconia (ZrO2) embedded in carbon nanowires via electrospinning for efficient arsenic removal from water combined with DFT studies, ACS Appl. Mater. Interfaces. 8 (2016) 18912–18921.

[40]. T. Yamashita, P. Hayes, Analysis of XPS spectra of Fe^{2+} and Fe^{3+} cations ions in oxide materials, Appl. Surf. Sci., 254 (2008) 2441-2449.

[41]. D. Sangalli, A. Debernardi, Exchange-correlation effects in the monoclinic to tetragonal phase stabilization of yttrium-doped ZrO2: A first-principles approach, Phys. Rev. B. 84 (2011) 214113.

[42]. A. Kambur, G.S. Pozan, I. Boz, Preparation, characterization and photocatalytic activity of TiO_2–ZrO_2 binary oxide nanoparticles, Appl. Catal. B Environ. 115 (2012) 149–158.

[43]. K. V. Kumar, K. Porkodi, F. Rocha, Langmuir–Hinshelwood kinetics–a theoretical study, Catalysis Communications, 9 (2008) 82-84.

[44]. Lahmar, H., Benamira, M., Akika, F. Z., &Trari, M. (2017). Reduction of chromium (VI) on the hetero-system $CuBi_2O_4/TiO_2$ under solar light.Journal ofPhysics andChemistry ofSolids, 110 (2017) 254–259

[45]. F.Z. Akika, M. Benamira, H. Lahmar, A. Tibera, R. Chabi, I. Avramova, Suzer, M. Trari, Structural and optical properties of Cu-substitution of NiAl2O4and their photocatalytic activity towards Congo red under solar light irradiation, J. Photochem. Photobiol. A Chem. 364 (2018) 542–550.

[46]. S. Douafer, H. Lahmar, M. Benamira, G. Rekhila, M. Trari, Physical and photoelectrochemical properties of the spinel LiMn2O4and its application in photocatalysis, J. Phys. Chem. Solids. 118 (2018) 62–67.

Tables captions:

Table 1. The calculated amount of the corresponding $ZrOCl_2 \cdot 8H_2O$ and $FeCl_3 \cdot 6H_2O$ used for the synthesis of 3 g of $Zr_{1-x}Fe_xO_{2-x/2}$ powders.

Table 2: Band gap energy and specific surface areas of the as-prepared powders.

Table 3: First-order kinetic constant (k_{app}) and R^2 under different initial concentrations of $HCrO_4^-$.

Figures captions:

Fig. 1. Powder X-ray diffraction results of $Zr_{1-x}Fe_xO_{2-x/2}$ (x=0.05, 0.10 and 0.5) powders.

Fig. 2. Scanning Electron Microscopy of $Zr_{1-x}Fe_xO_{2-x/2}$ (x=0.05, 0.10 and 0.5) prepared by co-precipitation method.

Fig. 3.a) FT-IR spectra of Zr1-xFexO2-x/2 (x=0.05, 0.10 and 0.5) prepared by the co-precipitation method, b) Enlargement of the region 500-900 cm^{-1}.

Fig. 4.XPS results of $Zr_{1-x}Fe_xO_{2-x/2}$(x=0.0 and 0.5) prepared by the co-precipitation method. a) XPS survey scan, b) O 1s of ZrO_2, c) O 1s of 50 mol% Fe-ZrO_2, d) Fe, e) Zr 3d.

Fig. 5.a) The diffuse reflectance spectrum of $Zr_{1-x}Fe_xO_{2-x/2}$ (x=0.05, 0.10 and 0.5). b) ZrO_2 and TiO_2. Inset the estimated direct band gap transition.

Fig. 6. a) Influence of the catalyst typeon the $HCrO_4^-$ photoreduction (30 mg/L, dose = 1 mg/mL, pH ~ 4, oxalic acid ~10^{-5} M T = 25 °C), b) UV–vis spectra of the chromate solution (30 mg/L) on the hetero-system 50 mol% Fe-ZrO_2/TiO_2).

Fig. 7.a) Effect of initial concentration of (VI) on the photo-reduction on the hetero-system 50 mol%Fe-ZrO_2/TiO_2 in the presence of oxalic acid (OA ~ 10^{-5} M, T = 25 °C, pH ~ 4, catalyst dose =1 mg/mL. b) Kinetics of the $HCrO_4^-$photoreduction. Inset: Plot of $1/k_{app}$ vs. C_o according to the modified L-H model.

Fig. 8. a) The Mott Schottky characteristic of 50 mol% Fe-ZrO_2 plotted in the working solution (pH ~ 4) at a frequency of 10 kHz. b) The thermal variation of the electrical conductivity

Fig.9. The energy band diagram of the hetero-system 50 mol% Fe-$ZrO_2/TiO_2/HCrO_4^-$ electrolyte.

Table 1. The calculated amount of the corresponding $ZrOCl_2 \cdot 8H_2O$ and $FeCl_3 \cdot 6H_2O$ used for the synthesis of 3 g of $Zr_{1-x}Fe_xO_{2-x/2}$ powders.

Samples $Zr_{1-x}Fe_xO_{2-x/2}$	x	$ZrOCl_2 \cdot 8H_2O$ (mol)	$FeCl_3 \cdot 6H_2O$ (mol)
ZrO_2	0.00	0.0243	0
5mol% Fe-ZrO_2	0.05	0.0235	0.0012
10 mol% Fe-ZrO_2	0.10	0.0227	0.0025
50 mol% Fe-ZrO_2	0.50	0.0148	0.0148

Table 2. Band gap energy and specific surface areas of the as-prepared powders.

Samples	Band gap energy, Eg (eV)	Specific surface area ($m^2\ g^{-1}$)
ZrO_2	4.01	25.25
TiO_2	3.21	30.21
$Zr_{0.95}Fe_{0.05}O_{1.975}$	2.15	29.30
$Zr_{0.9}Fe_{0.1}O_{1.95}$	2.00	30.02
$Zr_{0.5}Fe_{0.5}O_{1.75}$	1.77	31.88

Table 3: First-order kinetic constant (k_{app}) and R^2 under different initial concentrations of $HCrO_4^-$.

C_o (mg)	**30**	**45**	**60**	**75**	**90**
k_{app} (min^{-1})	0.0309	0.0141	0.009	0.0065	0.0038
R^2	0.991	0.996	0.994	0.992	0.976

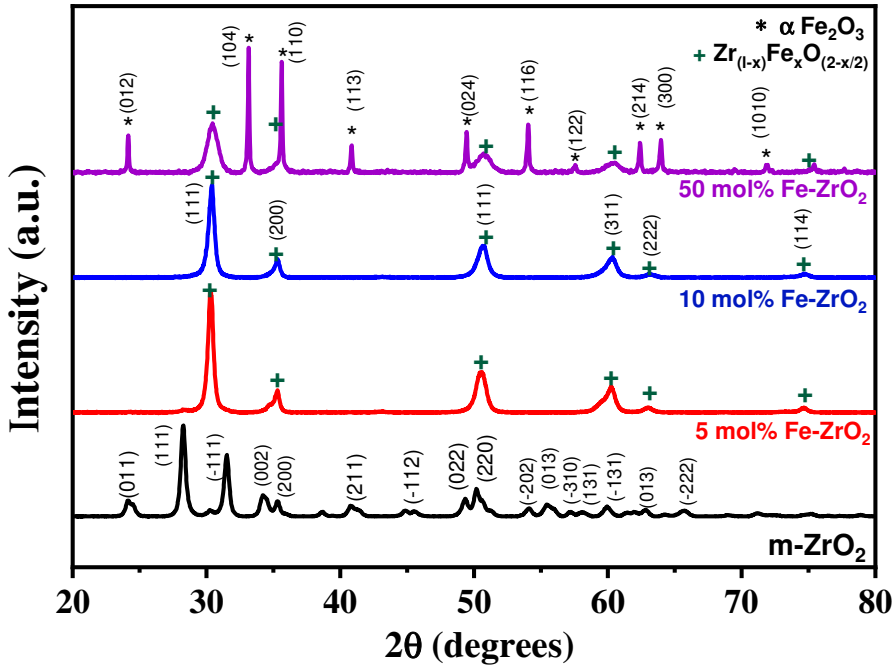

Fig. 1: Powder X-ray diffraction results of $Zr_{1-x}Fe_xO_{2-x/2}$ (x=0.05, 0.10 and 0.5) powders.

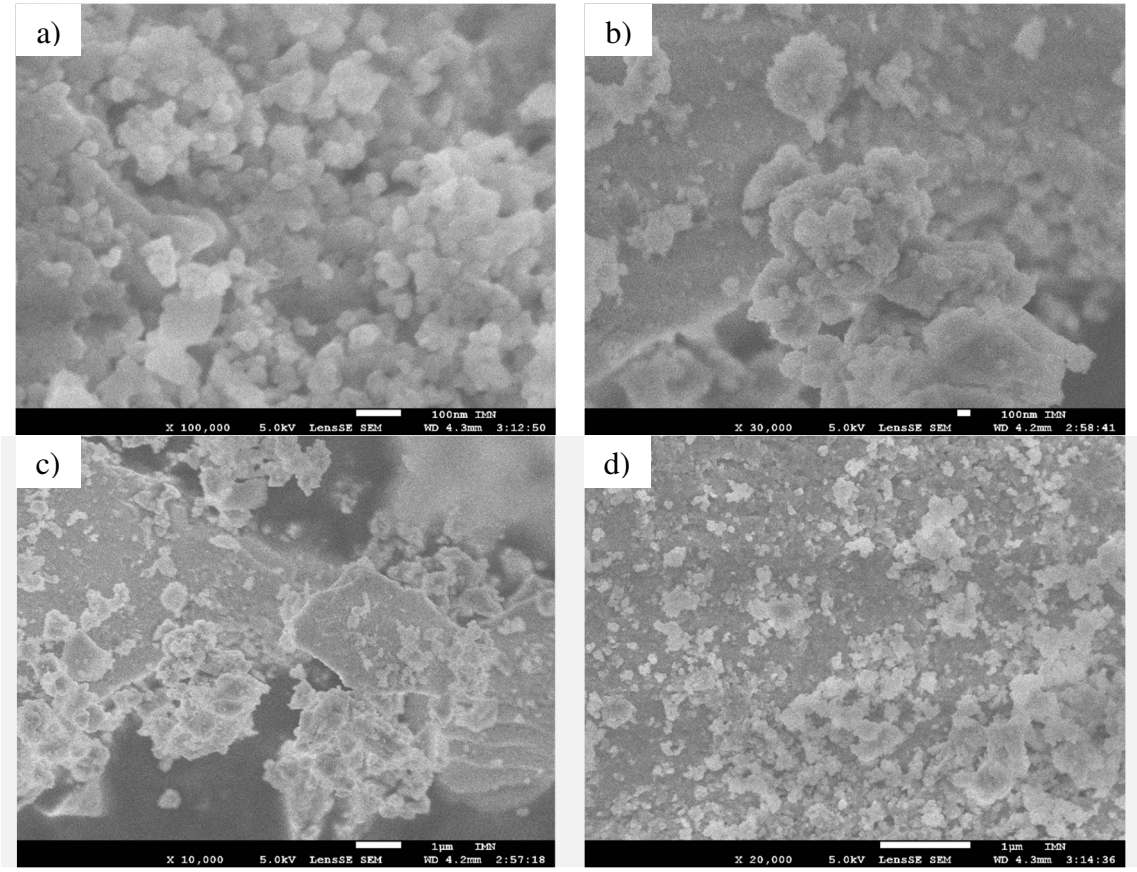

Fig. 2. Scanning Electron Microscopy of $Zr_{1-x}Fe_xO_{2-x/2}$: a) x=0, b) x=0.05, c) x=0.10 and d) x=0.5 prepared by co-precipitation method.

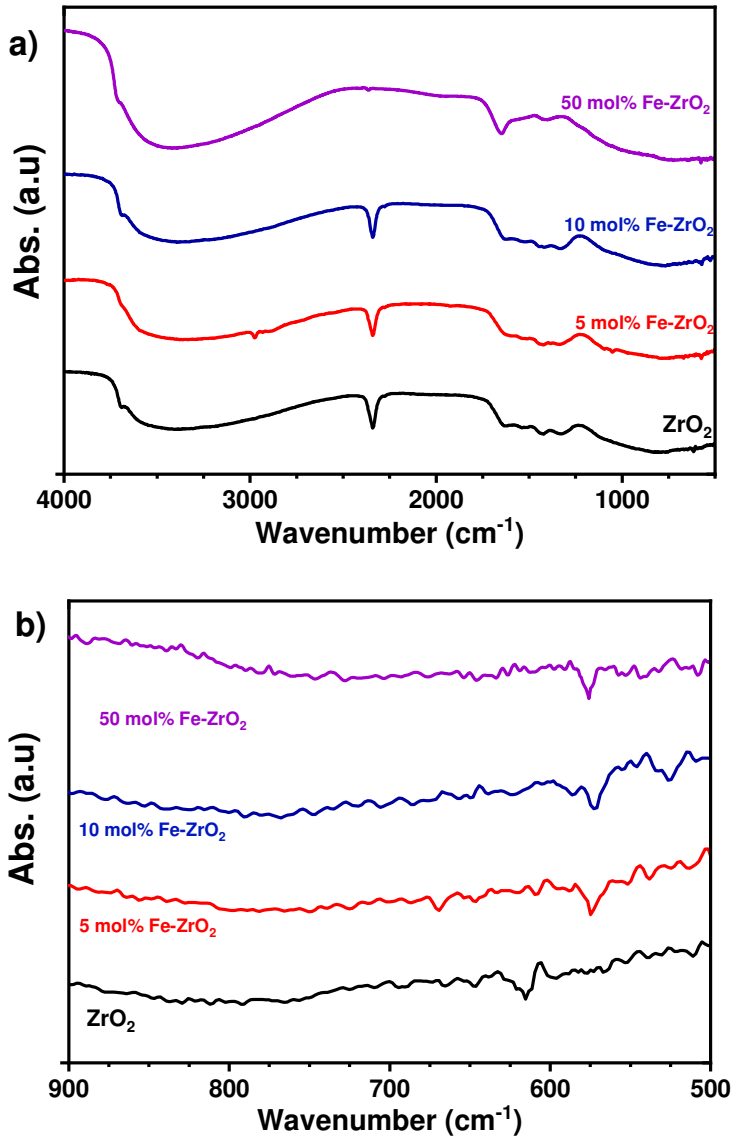

Fig. 3. a) FT-IR spectra of $Zr_{1-x}Fe_xO_{2-x/2}$ (x=0.05, 0.10 and 0.5) prepared by the co-precipitation method, b) Enlargement of the region 500-900 cm^{-1}.

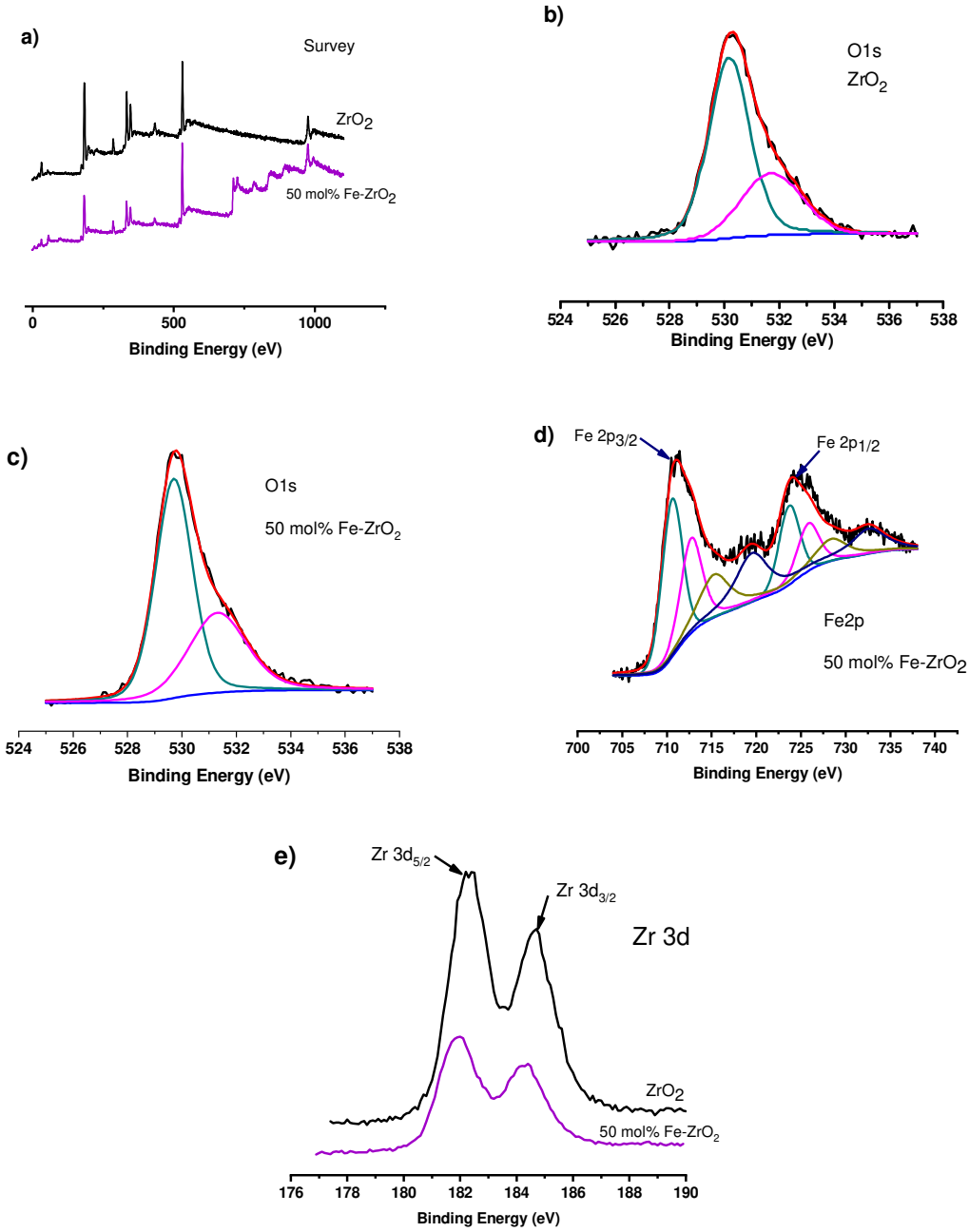

Fig. 4. XPS results of $Zr_{1-x}Fe_xO_{2-x/2}$ (x=0.0 and 0.5) prepared by the co-precipitation method. a) XPS survey scan, b) O 1s of ZrO_2, c) O 1s of 50 mol% Fe-ZrO_2, d) Fe, e) Zr 3d.

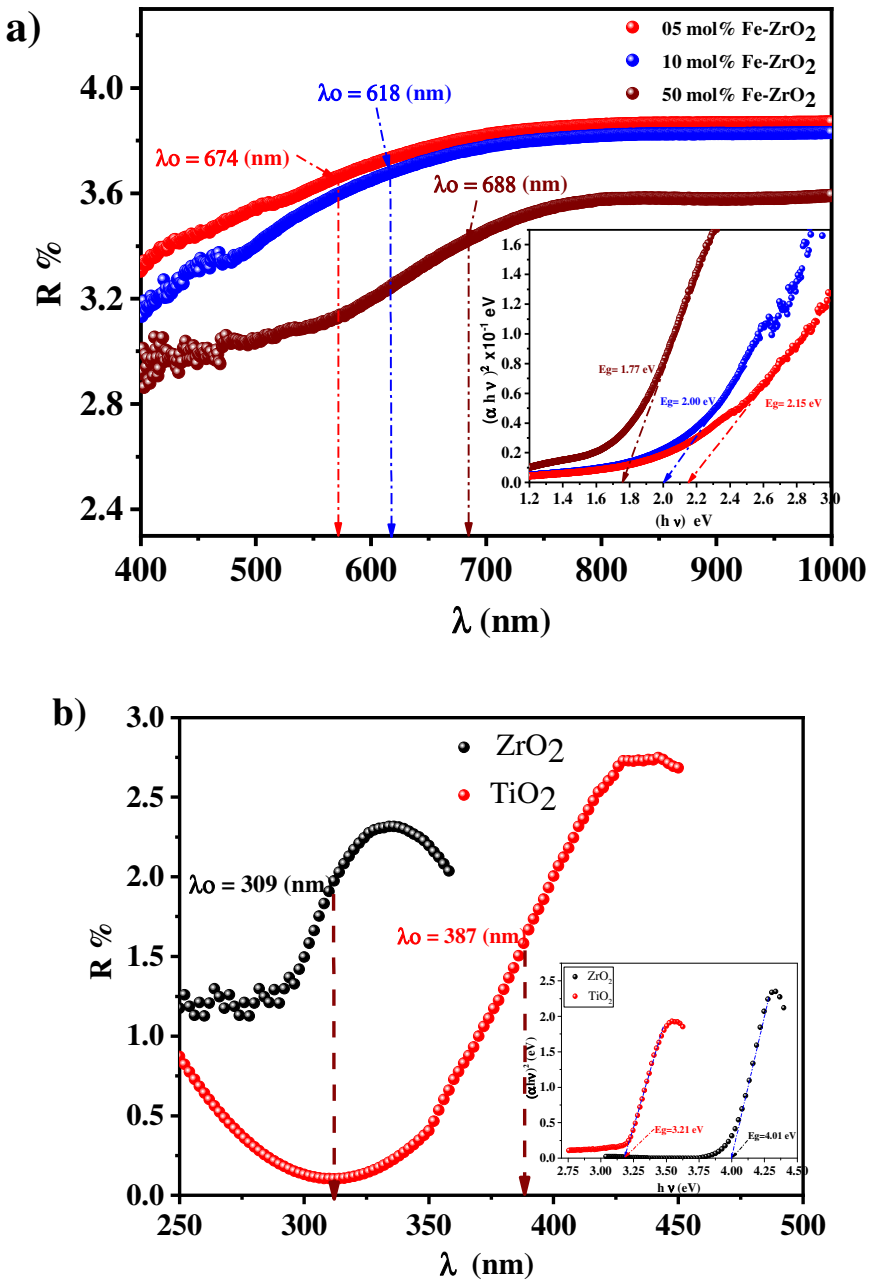

Fig. 5: a) The diffuse reflectance spectrum of $Zr_{1-x}Fe_xO_{2-x/2}$ (x=0.05, 0.10 and 0.5). b) ZrO_2 and TiO_2. Inset the estimated direct band gap transition.

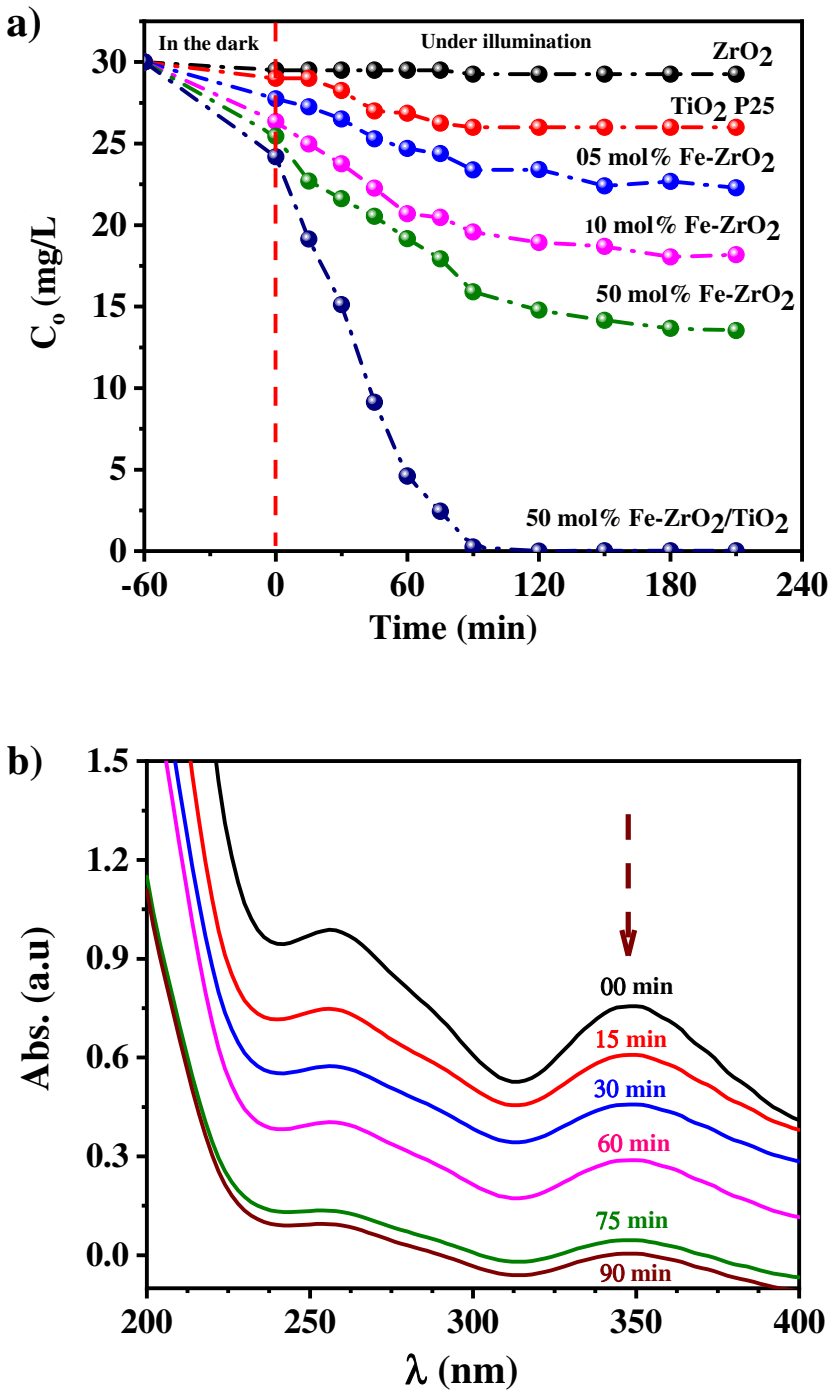

Fig. 6: a) Influence of the catalyst type on the $HCrO_4^-$ photo reduction (30 mg/L, Dose = 1 mg/mL, pH ~ 4, oxalic acid ~10^{-5} M, T = 25 °C), b) UV–vis spectra of the chromate solution (30 mg/L) on the hetero-system 50 mol% Fe-ZrO_2/TiO_2).

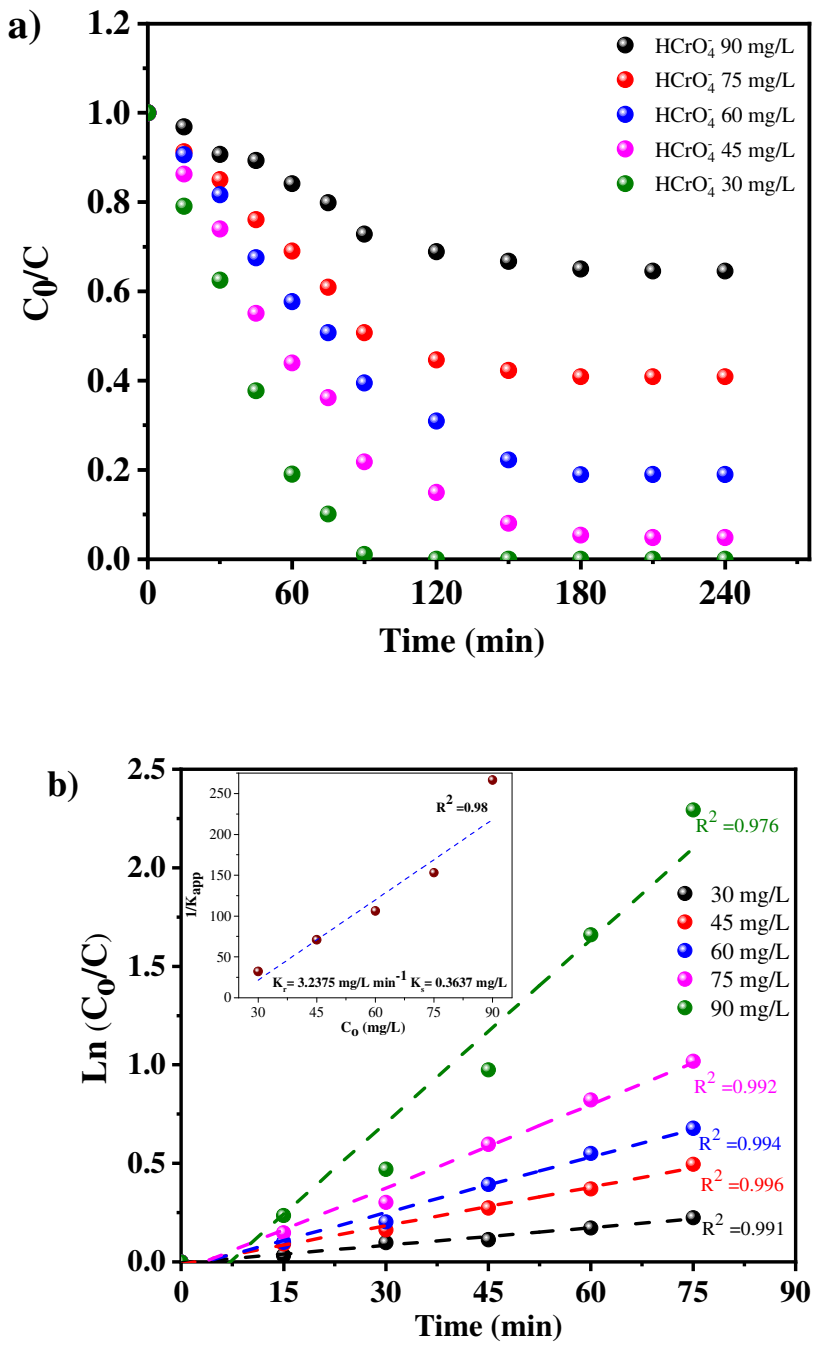

Fig. 7: a) Effect of initial concentration of chromium (VI) on the process of photo-reduction on the hetero-system 50 mol% Fe-ZrO_2/TiO_2 in the presence of oxalic acid (OA ~10^{-5} M, T = 25 °C, pH~ 4, catalyst dose =1 mg/mL. b) Kinetics of the $HCrO_4^-$ photoreduction. Inset: Plot of $1/k_{app}$ as a function of C_o according to the modified L–H model.

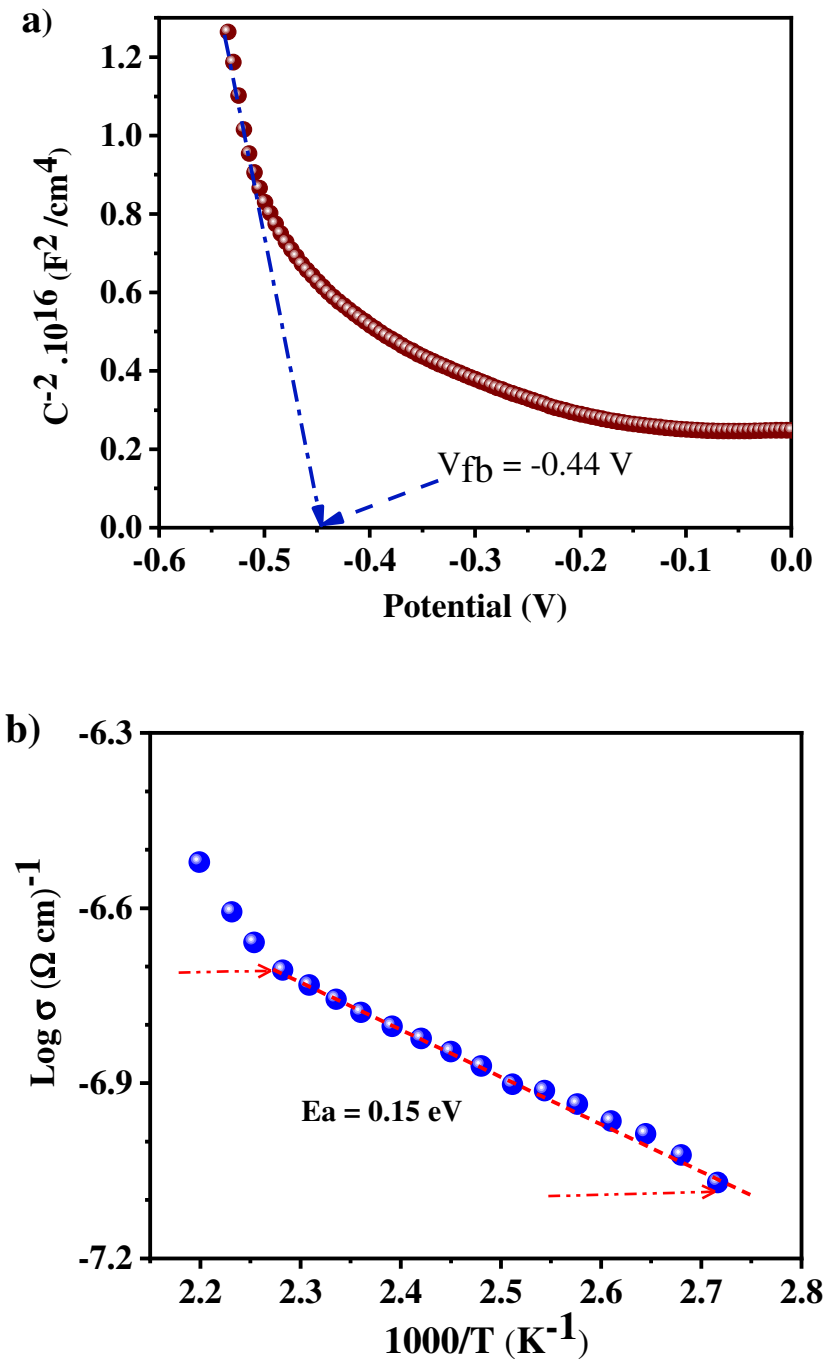

Fig. 8: a) The Mott Schottky characteristic of 50 mol% Fe-ZrO_2 plotted in the working solution (pH ~ 4) at a frequency of 10 kHz. b) The thermal variation of the electrical conductivity.

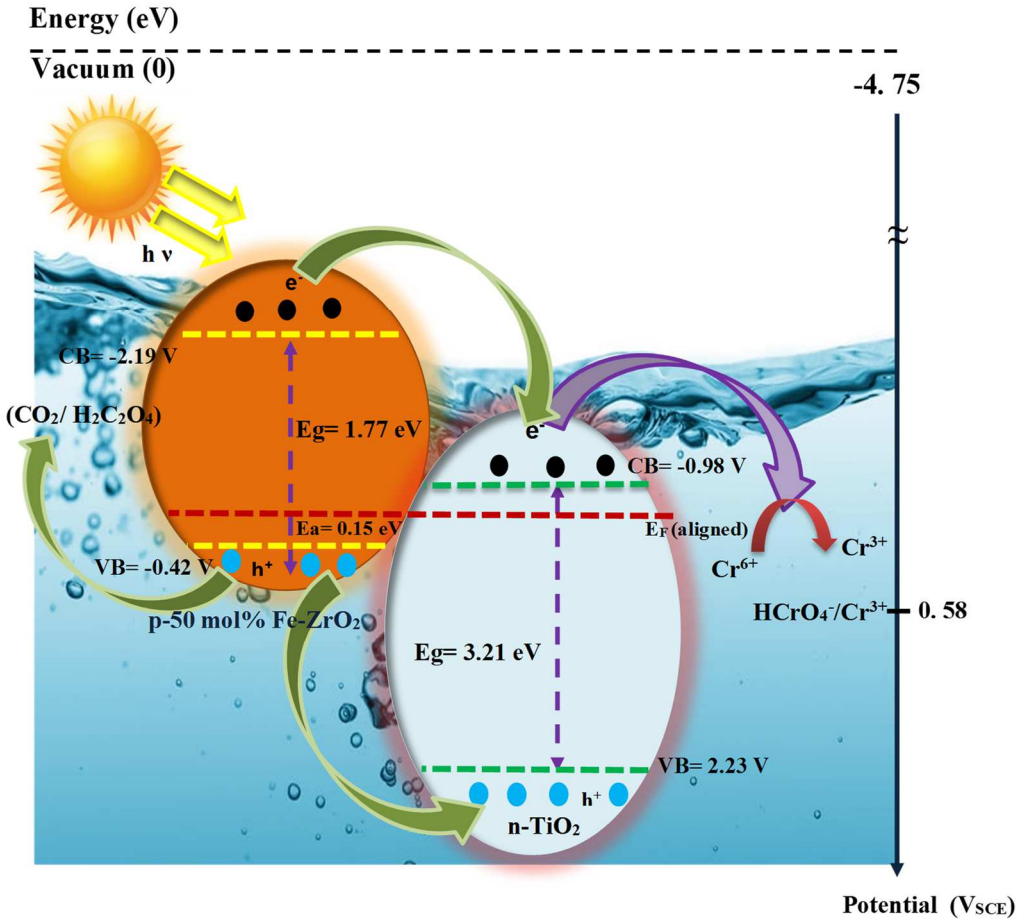

Fig. 9: The energy band diagram of the hetero-system 50 mol% Fe-ZrO_2/TiO_2/$HCrO_4^-$ electrolyte.

Graphical Abstract